Geochimica et Cosmochimica Acta 370 (2024) 66–77

Contents lists available at ScienceDirect

Geochimica et Cosmochimica Acta

journal homepage: www.elsevier.com/locate/gca

The geochemical evolution of basalt Enhanced Rock Weathering systems quantified from a natural analogue

T. Linke [a,*], E.H. Oelkers [a,b], K. Dideriksen [c,d], S.C. Möckel [e], S. Nilabh [f], F. Grandia [f], S. R. Gislason [a]

[a] Institute of Earth Sciences, University of Iceland, Sturlugata 7, 102 Reykjavik, Iceland
[b] Ali I. Al-Naimi Petroleum Engineering Research Center, KAUST, Saudi Arabia
[c] Nano-Science Center, Department of Chemistry, University of Copenhagen, 2100 Copenhagen, Denmark
[d] Geological Survey of Denmark & Greenland (GEUS), Øster Voldgade 10, 1350 Copenhagen, Denmark
[e] Institute of Life and Environmental Sciences, University of Iceland, Sturlugata 7, 102 Reykjavik, Iceland
[f] Amphos21, Carrer de Veneçuela, 103, 08019 Barcelona, Spain

ARTICLE INFO

Associate editor: Alexis Navarre-Sitchler

Keywords:
CO_2 storage
Alkalinity production
Basalt weathering
Heavy-metal mobility
Soil degassing
Enhanced rock weathering

ABSTRACT

Substantial quantities of fine-grained basaltic dust have fallen on South Iceland soils over at least the past 3300 years, making this region an ideal natural analogue to define the long-term consequences of current Enhanced Rock Weathering efforts. A relatively pristine South Iceland Gleyic/Histic Andosol, 3 m in height, receiving approximately 1250 mm of rainfall annually was selected for this study. This soil receives an estimated 500–800 g m^{-2} y^{-1} of basaltic dust. The soil waters in this system were regularly sampled as a function of depth from May to November 2018. The fluid pH, alkalinity and the concentrations of most major elements increased with depth as the fluids became more reduced. In contrast, whereas numerous toxic trace metals are initially released to the fluid by the dissolution of the basalt near the surface they are scavenged at depth likely due to their uptake by secondary minerals. Equilibrium reaction path modelling suggests that 1) the added airborne basaltic dust dissolves throughout the soil column and 2) in total 0.26 cm^3 of basalt dust dissolves per kg water in this soil–water system. Mass balance calculations indicate that the annual mass of basalt dissolved is less than 60 % of that added to the system, such that the mass of basaltic material in the soil column likely increases continuously over time. Basalt dissolution is maintained throughout the soil by the precipitation of Al-Si-minerals such as allophane, and organic anion ligands released from organic decay. These processes limit aqueous Al^{3+} activity and keep the soil waters undersaturated with respect to primary basaltic minerals and glass. The soil water pH is ~6 and has a higher alkalinity than that of both Icelandic surface waters and the ocean. In contrast, if no basalt was present, the pH of the soil solutions would be 4.4, with zero alkalinity, illustrating the role of added basalt in drawing CO_2 out of the atmosphere.

1. Introduction

Enhanced Rock Weathering (ERW) is currently being explored as a method to remove CO_2 directly from the atmosphere to limit future global warming (e.g., Schuiling and Krijgsman, 2006; Hartmann et al., 2013; Moosdorf et al., 2014; Edwards et al., 2017; Beerling et al., 2018; Dietzen et al., 2018, IPCC, 2018; Haque et al., 2021; Paulo et al., 2021; Kantzas et al., 2022; Baek et al., 2023; Deng et al., 2023; Reershemius et al., 2023). This process involves amending soils with crushed fast-reacting Ca-Mg-silicate rocks and minerals such as basalt (Haque et al., 2019a, 2020; Beerling et al., 2020). To date these studies have been short-term, lasting for no more than 5 years (Haque et al., 2019a; Goll et al., 2021). Consequently, the long-term consequences of enhanced weathering efforts are poorly constrained. The present study was motivated to illuminate the longer-term consequences of Enhanced Rock Weathering efforts through a detailed characterization of the geochemistry of an analogue field site located in South Iceland.

The natural analogue considered in the present study in South Iceland is a Gleyic/Histic Andosol (Arnalds, 2015). Gleyic and Histic Andosols are soil classes and correspond to Aquands in Soil Taxonomy. Andosols are mineral soils derived from volcanic sediments and cover about 2 % of the Earth's terrestrial surface (Arnalds, 2015). Andosols

* Corresponding author.
E-mail address: tol5@hi.is (T. Linke).

https://doi.org/10.1016/j.gca.2024.02.005
Received 19 September 2023; Accepted 8 February 2024
Available online 16 February 2024
0016-7037/© 2024 The Author(s). Published by Elsevier Ltd. This is an open access article under the CC BY license (http://creativecommons.org/licenses/by/4.0/).

store about 5 % of the terrestrial carbon (Eswaran et al., 1993). The Andosols of South Iceland receive frequent basaltic dust fallout; the mass of basaltic dust added to these soils is estimated to be 500 to 800 g m^{-2} y^{-1} (Arnalds, 2010; Arnalds et al., 2014, 2016). In addition, less frequent and larger grained airborne volcanic material is transported during explosive volcanic eruptions in the form of glassy volcanic ash fallout referred to as *tephra*. The tephra forms distinct horizons that can be used to date the soil as a function of depth. In total it is estimated that up to 800 g m^{-2} y^{-1} of natural basaltic dust has been added to the soils in South Iceland for the past 3300 years. In contrast, enhanced rock weathering experiments to date have added up to 40 kg m^{-2} of crushed Ca-Mg-silicate rocks to agricultural soils annually (Gillman et al., 2002; Cho et al., 2010; ten Berge et al., 2012; Amann et al., 2018; Haque et al., 2019b). Due to the long regular addition of natural basaltic dust to South Icelandic soils, these soils likely provide an insightful natural analogue to illuminate the long-term effect of adding ground basalt to soils as part of enhanced rock weathering efforts.

This is the first manuscript exploring the long-term efficiency and consequences of enhanced rock weathering efforts through the study of a South Iceland Gleyic/Histic Andosol. Future manuscripts will present an estimate of the rate of alkalinity generation and carbon drawdown due to the addition of basaltic dust to this Gleyic/Histic Andosol. In this article we report the composition of fluids and solids in our studied South Iceland soil as a function of depth and time over two field seasons. These observations were used together with geochemical modelling calculations to 1) quantify the saturation state of the primary and secondary mineral phases with respect to the soil solutions, 2) to determine the processes controlling the mobility of heavy metals, and 3) assess the rate at which basalt dissolved in the soils.

2. Methods

2.1. Field site description

The field site chosen for this study is located approximately 7 km north from the town of Hella, at the headwaters of the Rauðalækur river in South Iceland (Fig. 1A). This site was selected as an analog to understand the long-term behavior and consequences of current ERW efforts. There are a number of reasons why these soils provide an excellent natural analogue for ERW systems. First, due to annual dust fallout, these soils have received over 16,500 t ha^{-1} of basaltic dust over the past 3300 years. Second, the specific surface area of natural basaltic dust is likely substantially higher than that added to the soils in current ERW experiments due to its finer grain size. The grain size of the crushed rocks used in ERW-applications, if reported, is commonly less than 150 μm (Gillman et al., 2002; Haque et al., 2019b). In contrast, the average size of basaltic Icelandic dust ranges from 10 to 62 μm (Arnalds et al., 2014; Liu et al., 2014; Baldo et al., 2020).

The area upstream of the field site has not been used for agriculture nor fertilized during the past several decades and is therefore considered to be in a natural state. Some drainage channels have been cut in the region, the closest located around 150 m from the study site. The soil at this site is organic-rich and receives substantial and regular input of aeolian basaltic material. Tephra layers from past volcanic eruptions are visible in an outcrop wall located about 10 m downstream from the suction cup lysimeters used in this study (see Fig. 1B). These tephra layers can be used to date the soil profile.

2.2. Soil water, soil sampling and field measurements

Soil water samples were collected using suction cup lysimeters provided by Prenart Denmark. These lysimeters were installed 10 m upstream from a southwest facing outcrop wall and placed at depths of 76, 121, 173 and 260 cm from the surface. Collected fluid samples were analyzed for pH, temperature, dissolved H_2S concentration and redox potential in the field. The dissolved H_2S content was measured by precipitation titration immediately after sampling with an uncertainty of ±0.7 μmol kg^{-1}_{water}, using mercury acetate solution $Hg(CH_3COO)_2$ as described by Arnórsson (2000). The redox potentials were measured using an Ag/AgCl micro redox electrode. Measured values were converted to equivalent potentials for a standard hydrogen electrode (E_{SHE}) using a value of +199 mV for the reference potential E° of the Ag/AgCl electrode (Sawyer et al., 1995) via the Nernst equation. Additional fluid samples were filtered through 0.2 μm cellulose acetate in-line filters for major element and alkalinity measurements in the laboratory. For major element analysis, 10 ml of soil water collected from each level was transferred into acid washed polypropylene bottles and acidified to 0.5 % HNO_3 using concentrated Merck suprapure 65 % HNO_3. Samples for iron speciation determination were collected into acid washed polypropylene bottles and acidified to 0.5 % HCl using Merck suprapure HCl.

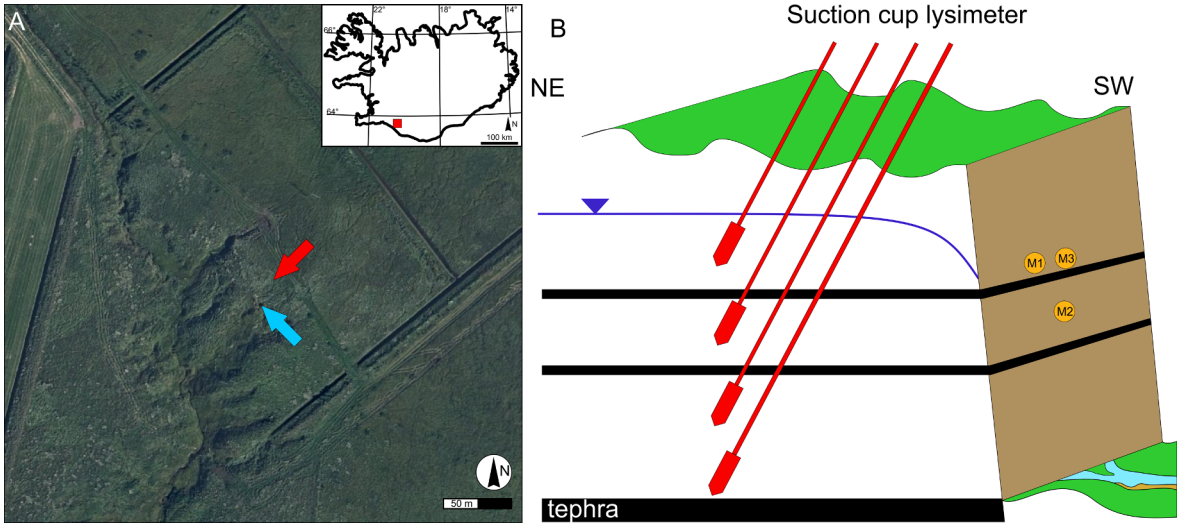

Fig. 1. A: Aerial photo of the studied field site and sampling locations, the red arrow shows the location of suction cup lysimeters and the orange arrow shows the location of the natural outcrop where solid samples were collected. Straight lineation's on the photo are man-made drainage channels (aerial photo published with permission from Loftmyndir ehf). **B:** Schematic NE-SW cross section of the studied outcrop and the position of suction cup lysimeters (shown in red). The locations of soil core samples collected from horizons at 71–96 cm and 120 cm depths are shown as orange dots (labeled M1, M2 and M3). Black horizontal lines represent tephra layers, and the blue curve illustrates the estimated position of the groundwater table.

Samples for dissolved organic carbon (DOC) measurement were collected in 30 ml acid washed polycarbonate bottles and acidified with 0.5 M Merck suprapure HCl to 1:30 ratio. Alkalinity titrations were performed after returning to the laboratory by titrating fluid samples, while constant stirring to pH 3.3 using 0.1 M HCl. The alkalinity was then calculated via the Gran method (Gran, 1952) with an uncertainty of ±5 % or less. A detailed description of the analysis methods is provided in section 2.3.

Solid soil samples were collected in May 2017 from the cleared face of the outcrop wall, located 10 m from the suction cup lysimeters (see Fig. 1B). Soil cores were obtained by pushing 7.5 cm diameter, 30 cm long PVC tubes horizontally into the outcrop, which were then sealed to prevent oxidation. The sample tubes were subsequently opened in the laboratory, inside a glove box under an anoxic atmosphere consisting of 97 % N_2 and 3 % H_2. Palladium catalysts were present in the glove box to remove traces of O_2 and minimize sample oxidation. Material from the inner parts of the cores was prepared for powder X-ray diffraction analysis (XRD) in a Bruker dome sample holder. The prepared samples were analyzed immediately after their preparation using a Bruker D8 Advance Plus X-ray diffractometer with 2θ geometry equipped with a copper X-ray source (λ = 0.15406 nm) and a Ni-filter. The samples were measured over the 5-70° 2θ range with a step size of 0.02° 2θ and a counting time of 1.2 s per step. Additionally, some of the sample material was dried in the glove box and then analyzed by powder X-ray diffraction as described above.

Pair distribution function PDF analysis was performed on the soil samples to further characterize the structure of amorphous or cryptocrystalline phases. The samples were first dried and then loaded into Cole-Parmer polyimide capillaries. Measurements were performed as described by Dideriksen et al. (2015) at Beam line 11-ID-B of the Advanced Photon Source, Argonne National Laboratory using X-rays with an energy of 58.6 keV. To calibrate and convert data from 2D to 1D we used the program fit2D (Hammersley et al., 1996; Hammersley, 1997). Further data processing was performed using PDFgetX2 (Qiu et al., 2004). Pair distribution functions, G(r), were generated by Fourier transformation using a Q_{max} of 24 $Å^{-1}$ and are provided together with the X-ray scattering data I(Q). The PDFgetX2 data treatment requires definition of the chemical composition of the samples. To obtain these compositions, preliminary SEM/EDX analyses were performed. These showed a pronounced Fe and O signal with less pronounced Si and C signals. Based on these results, it was assumed that the soil samples had a composition consistent with:

$$SiO_2 + x\ Fe(OH)_3 + y\ H_2O + z\ CH_2O \quad (1)$$

The value of *x* in Equation (1) was estimated from the relative peak intensities at ~1.6 Å, corresponding to Si—O, and at ~2 Å for Fe(III)-O or ~2.1 Å for Fe(II)-O, taking into account the difference in electron density and expected coordination number of SiO_4 and FeO_6. The values of *y* and *z* in equation (1) were subsequently defined by trial and error to avoid high amplitude oscillations in the G(r) function at low r values. Tests of the procedure on the same samples yielded highly similar PDF fits at r >1 Å with values of *x* varying within ±30 %.

2.3. Analytical Techniques

Major element concentrations were analyzed in duplicate using a Ciros Vision, Spectro Inductively Coupled Plasma Optical Emission Spectrometer (ICP-OES). The same subsamples were used to measure the trace element compositions of fluid samples using a Thermo iCAP Qc Inductive coupled plasma mass spectrometer (ICP-MS). Prior to the analysis the samples were diluted with milliQ water and spiked with internal Rh, Ir, and Ga standards to correct measurements for detector drift. For both ICP-OES and ICP-MS measurements, the uncertainties were below ±5 % for all elements. Iron redox species were determined using a Dionex 3000 ion chromatography system using the method described by Kaasalainen et al., (2016). DOC concentrations were determined by size exclusion chromatography using a Liquid Chromatography – Organic Carbon Detection system (LC-OCD) following the method of Huber et al. (2011).The limit of quantification (LOQ) for each element is presented in S1.

2.4. Geochemical Modelling

In-situ aqueous speciation, charge balance, mineral saturation states and equilibrium reaction paths were modelled using the PHREEQC interactive software version 3.4.0 (Parkhurst and Appelo, 1999). Calculations were performed using the minteq.v4.dat (Allison et al., 1991; U.S. Environmental Protection Agency, 1998) database after adding to it the thermodynamic data for minerals, aqueous species and glasses listed in electronic supplement S2.

Based on these calculations, predominance diagrams were plotted using PhreePlot (Kinniburgh and Cooper, 2004) as described in Linke and Gislason (2018). Hematite, magnetite, goethite, were not allowed to form making ferrihydrite and siderite the most stable Fe phases in the modelled system that form as a result of weathering process at the surface. These two minerals have been identified in the studied field site. Note that Baldo et al. (2020) identified hematite, goethite, and magnetite in Icelandic dust. Neither these minerals nor maghemite and lepidocrocite were observed to form in our field area nor the field observations reported by Arnalds (2004). Geochemical modelling was also used to assess the saturation state of the soil solutions with respect to atmospheric CO_2 and O_2, selected minerals and glasses.

2.4.1. Reaction path modelling

Equilibrium reaction path modelling was performed in the present study using PHREEQC. The initial fluid compositions entering the soil used in the modelling was set to the average composition of South Iceland rainwater as provided in Table S3 (Eiriksdottir et al., 2014). The composition of the dissolving basalt was based on the chemical analysis of volcanic rocks located close to the study area (Harðardóttir, 2020) comprising the most likely source for the dust added into the studied soils (Arnalds et al., 2014, 2016). The composition of this basalt is provided in Table S2 and its metal oxide composition is provided in Table 1. The dissolution reaction of this 'On-Site' basalt can be written as:

$$SiAl_{0.335}Fe_{0.265}Mg_{0.165}Ca_{0.22}Na_{0.12}K_{0.019}O_{3.222} + 1.104H^+ + 2.118H_2O = H_4SiO_4 + 0.335Al(OH)_4^- + 0.265Fe^{2+} + 0.165\ Mg^{2+} + 0.22Ca^{2+} + 0.12Na^+ + 0.019\ K^+ \quad (2)$$

Equilibrium reaction path models were used to calculate the fluid composition and mass of minerals precipitating from the fluid phase as this basalt dissolves into the fluid. Based on field observations, only the upper 70 cm of the soil column is assumed to be oxic with the uppermost part in equilibrium with atmospheric oxygen. No oxygen source is present deeper in the soil. The initial rainwater is set to be in equilibrium with atmospheric CO_2 and oxygen. As Fe^{2+} dominates the oxidation state of iron in the 'On-Site' basalt, all iron released from this basalt was assumed to be in this oxidation state. During the simulations, O_2 is

Table 1
Metal oxide composition of the 'On-Site' basalt used for data interpretation in this study. Note for simplicity all iron is shown as Fe^{2+}.

metal oxide	Mass-%
SiO_2	50.15
Al_2O_3	14.26
FeO	15.89
MgO	5.55
CaO	10.3
Na_2O	3.1
K_2O	0.75

continuously removed from the system as Fe^{2+} is released from the dissolving basalt and oxidized. The partial pressure of CO_2 in the soil is set to 0.05 bar, which is the average of that measured in the soil water samples. The effect of the presence of DOC in the model calculations was taken into account by assuming that all DOC was present as aqueous oxalate. This choice was made because oxalate is representative of aqueous organic species and because of the availability of equilibrium constants for aqueous metal-oxalic complexes (Pettit and Powell, 2008).

The minerals allowed to precipitate in the reaction path models were restricted to include only those observed in andosols, namely ferrihydrite and allophane. In addition, a silica phase with thermodynamic properties of moganite was included. Under reduced conditions allophane, moganite, siderite and mackinawite were allowed to precipitate at local equilibrium if these phases became supersaturated. The mass of basalt dissolved was tuned to best fit the Ca and Mg concentration observed in the field. The model, however, does not include provision for bacterial activity or local compositional, physical, or mineralogical heterogeneities.

3. Results

3.1. Mineral and chemical composition of the collected solids

X-Ray diffraction (XRD) analysis and Pair Distribution Function (PDF) analysis were conducted to determine the mineralogical composition of the soil samples. The XRD pattern of the soil, as shown in Fig. 2A, exhibits a strong background at 10° to 20° 2θ caused by the dome sample holder used to protect the samples from oxidation and at 30° and 60° 2θ by the presence of amorphous and/or poorly crystalline material that cannot be identified by XRD. Additional minor amounts of crystalline feldspar and pyroxene are present. Material collected from a soil horizon between 71 and 96 cm in depth (Fig. 1B) contains crystalline siderite (Fig. 2B). No difference in the mineral composition or relative peak intensity was observed between the wet samples measured in the dome sample holders and corresponding material dried in the glove box. Red material collected from the same horizon as the siderite does not show distinct XRD peaks, but Pair Distribution Function analysis indicates that it contains a short range ordered ferrihydrite, indicated by peaks at e.g., 2.0 Å for Fe-O pairs, at 3.1 Å for edge sharing Fe-Fe pairs and at 3.4 Å for corner sharing Fe-Fe pairs (Fig. 2C and Fig. 2D).

3.2. Fluid Compositions

Soil water samples were analyzed for their major and trace metal composition as well as for redox sensitive elements and dissolved organic and inorganic carbon. All measured compositions are provided in Tables S1 and S4. These compositions were recalculated to the *in-situ* soil temperature of 7 °C, the average soil temperature at 76–260 cm depth during the summer months (Petersen and Berber, 2018), using PHREEQC (Parkhurst and Appelo, 1999). These recalculated fluid compositions are shown as a function of depth in Figs. 3 and 4.

The redox potential (Eh_{SHE}), the logarithmic partial pressure of the CO_2, and the dissolved inorganic carbon (DIC) concentrations of the soil water samples are shown in Fig. 3. For comparison, the redox potential was also calculated based on measured concentrations of Fe^{2+}/Fe^{3+} and of SO_4^{2-}/HS^- using PHREEQC. These values are compared to the Eh measured in the field in Fig. S5 in the Electronic Supplement. In general, the closer the samples are to the atmosphere, the more oxic the soil water samples.

The redox potential of the soil water samples, Eh_{SHE}, decreases with increasing depth and pH. There are significant variations in pH, Eh_{SHE} and pCO_2 with time at each soil depth. Although no clear trend for temporal pH evolution is evident, the measured Eh increased in all soil water samples during October and November likely due to changes in bacterial activity. The alkalinity of the fluid samples increased during the summer months, peaking in mid-September, it declined thereafter (see Table S4).

The concentrations of DIC and Si are relatively high compared to other constituents, reflecting basalt dissolution and organic matter decomposition. Average DIC concentration increases with increasing depth but varies seasonally (see Fig. 3 and Fig. S1). The highest DIC concentration was found in samples collected during September, except for the deepest samples collected at 260 cm depth, where this concentration peaked later in the fall. DOC concentrations increased with time during the summer and fall and have the lowest concentrations at the greatest depths. The DOC concentrations are generally 7–21 times lower than the DIC concentrations. The variations in DIC and DOC over time are likely caused by the response of bacterial activity and organic decay to seasonal changes in temperature and environmental conditions. There are significant temporal variations in measured Si concentrations at depths of 76 cm and 121 cm. Deeper in the soil, the Si concentrations

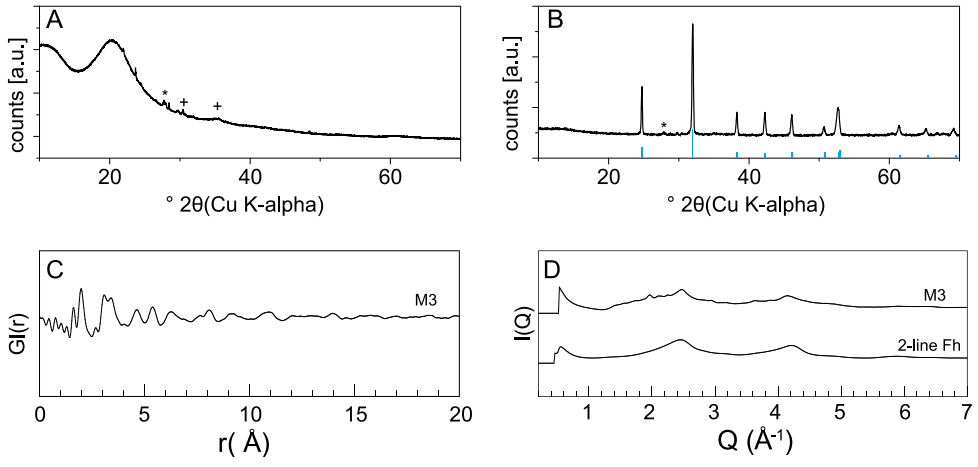

Fig. 2. A: Representative Powder X-ray Diffraction (XRD) pattern of a soil sample collected from ~120 cm in depth. The small peaks indicated by the * and +symbols are consistent with feldspar and pyroxene, the major crystalline phases in basalt. The high background is caused by the dome sample holder and the presence of amorphous and nanocrystalline material. **B:** Powder X-ray diffraction pattern of a dried nodule identified as siderite collected from ~80 cm in depth. All major peaks correspond to the siderite reference pattern; the siderite peaks shown with relative intensity as blue bars were reported by Effenberger et al. (1981). The additional peak indicated with a * at 27.9° 2 θ corresponds to the main peak of Ca-rich feldspar. **C:** Pair Distribution function (G(r)) in real space of red solid material collected from the outcrop wall at ~80 cm depth. This is identified as a ferrihydrite-rich soil. The absence of larger peaks at >15 Å indicates the short order of the mineral phase. **D:** X-ray scattering data, I(Q), of red material collected from the outcrop wall at ~80 cm in depth. Also shown is the I(Q) of a 2-line ferrihydrite standard. The natural sample with minor impurities resembles closely the ferrihydrite standard material.

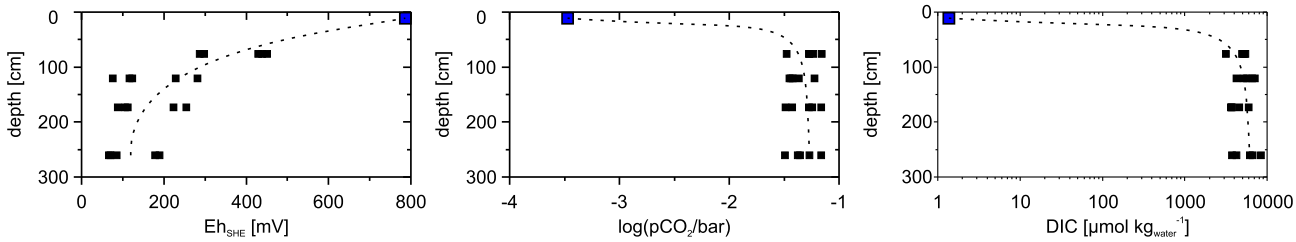

Fig. 3. The redox state, Eh_{SHE}, the logarithm of the partial pressure of CO_2, $log(pCO_2/bar)$, and the dissolved inorganic carbon (DIC), in log scale, at each sampling depth for all collected fluid samples and for rainwater (plotted as a blue square). Dashed lines show the trend of the data with increasing soil depth.

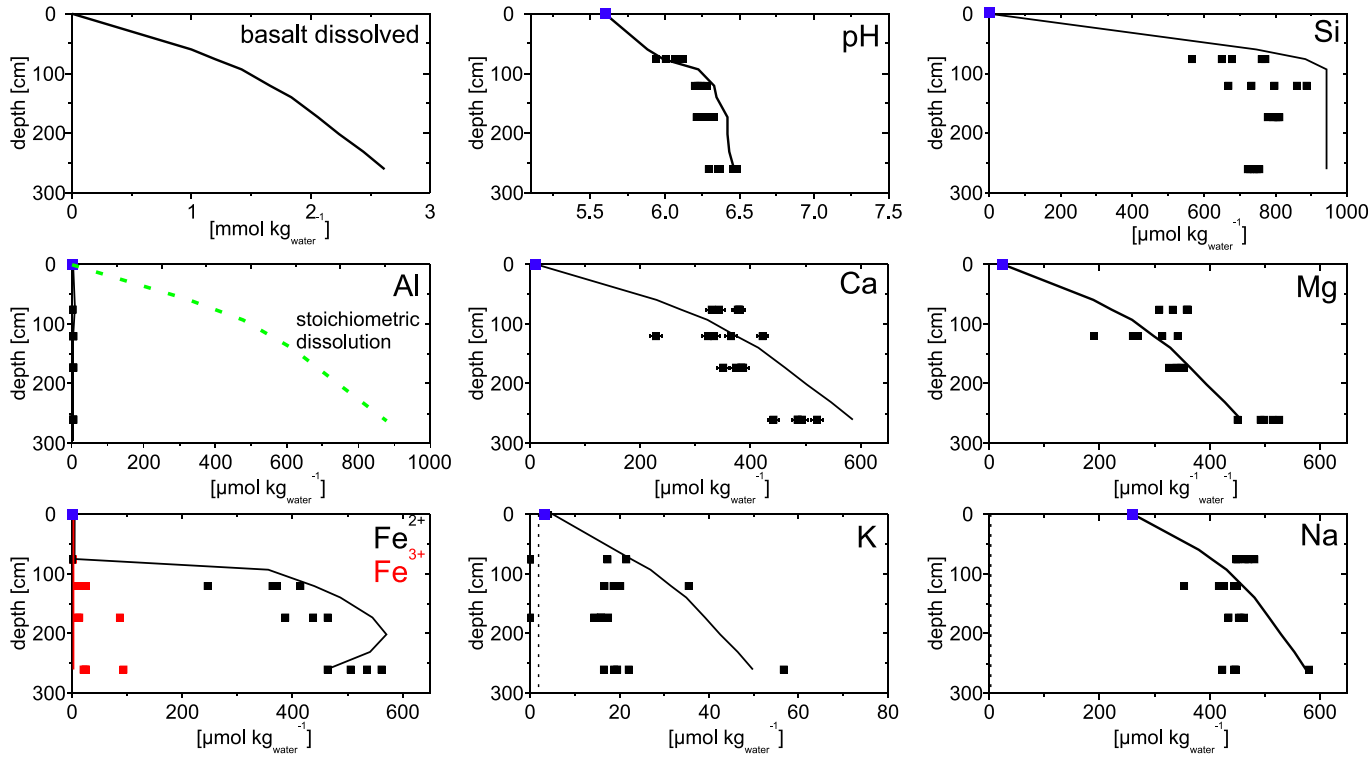

Fig. 4. Evolution of major dissolved constituents in sampled soil water as a function of depth. The black and red symbols correspond to measured soil water concentrations, the blue symbols represent the composition of rainwater, and the solid curves show the results of modelling calculations (see text). Note the different concentration scales for each constituent. Also shown as a green dashed curve are the calculated Al concentrations determined assuming stoichiometric dissolution of basalt in the absence of secondary mineral precipitation. The iron species are shown as red and black squares depending on the measured oxidation state of the iron. The iron concentration is close to the detection limits in the shallowest soil water samples at 76 cm depth, causing the symbols to appear as a single square, and the modelled concentrations of Fe^{3+} and Fe^{2+} at shallow levels are ±0 µmol kg_{water}^{-1}. Dashed lines represent limit of quantification, and uncertainties are within symbol size except for Ca.

vary less over time (Fig. 4).

The concentrations of all other elements are lower than those of Si. The Al concentrations, as shown in Fig. 4, range from below the 0.28 µmol kg_{water}^{-1} quantification limit to 3 µmol kg_{water}^{-1}. This is ~200 times lower than the corresponding measured Si concentrations. The concentrations of Mg, Ca, Fe, Mn, Sr, and Ti generally increase with depth and their concentrations suggest the close to stoichiometric dissolution of the basalt in the soil. Only 10 to 20 % of the total dissolved iron is present as Fe^{3+}. At 76 cm depth, under oxidizing conditions, the concentrations of both Fe^{2+} and Fe^{3+} are close to the detection limit. Manganese concentrations exhibit the same trend as iron, being only present as reduced Mn^{2+} deeper in the soil, where anoxic conditions are present. The concentrations of Cl, Na and K do not correlate with depth, as these concentrations are largely controlled by their concentrations in the influent rainwater.

The soil water H_2S concentration increases with depth, while total S decreases (Fig. 5). The concentrations of the trace metals Cd, Co, Cu, Mo, Ni, and Pb also decrease with depth (see Fig. 5 and Table S1). The similarity of these behaviors suggests consumption of these trace metals by secondary sulfide mineral precipitation (e.g., Charriau et al., 2011; Smieja-Król et al., 2015) The concentrations of other metals including As and Cd are close or below the detection limit in all collected water samples and Pb is only above the limit of quantification in one shallow soil water sample.

An Eh-pH diagram illustrating the stability of iron phases at the conditions of our field site is shown in Fig. 6. The pH of the soil water samples increases continuously with depth as the samples become more anoxic. At shallow levels the oxidized Fe^{3+} species are dominant, which lead to a supersaturation of the fluid phase with respect to ferrihydrite at these depths. Deeper in the soil Fe^{2+} dominates. The dissolved iron concentrations increase with depth and up to ~500 µmol kg_{water}^{-1}. As a consequence, the water approaches equilibrium with respect to siderite. The sulfur concentrations of the sampled soil waters at depth greater than 121 cm did not exceed 80 µmol kg_{water}^{-1}. No sulfide minerals are

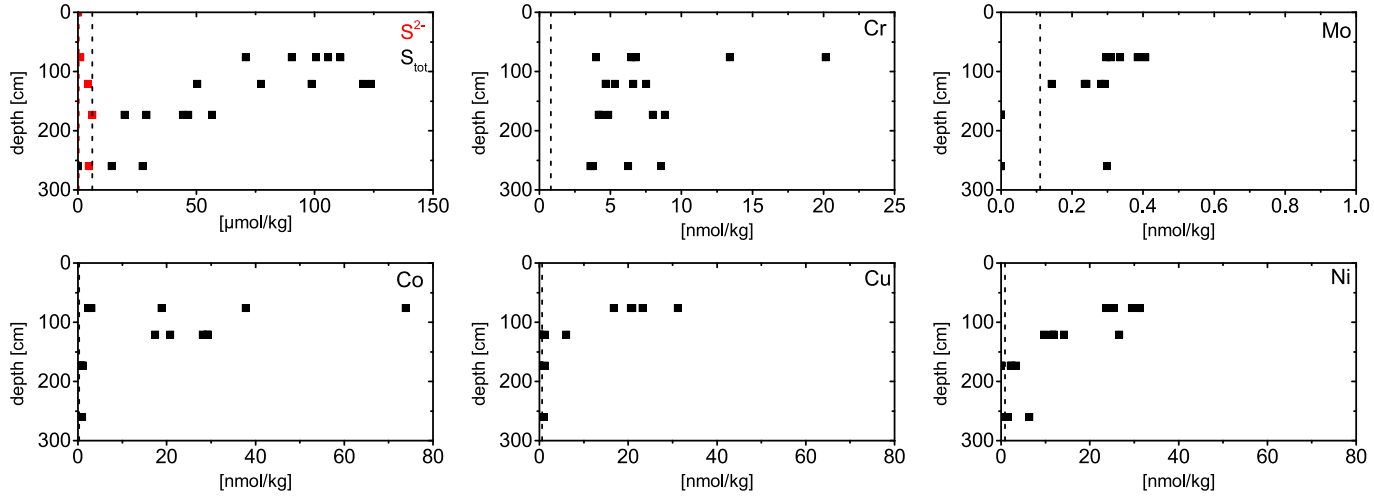

Fig. 5. Sulfur and trace metal concentrations in soil water samples versus depth. Note the different units and scales on the horizontal axes. Black dashed lines represent Limit of quantification. Uncertainties are within symbol size.

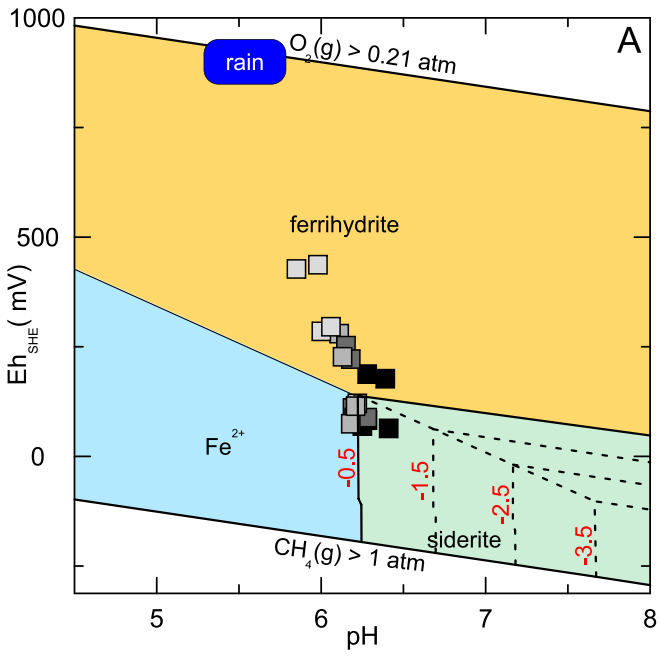

Fig. 6. Eh-pH diagram computed with PhreePlot illustrating the predominance fields of iron phases as at a temperature of 7 °C. The square symbols show the composition of collected soil water samples. The shading of the symbols indicates the depth of the water sample; the darker the shading, the deeper the sample. The black lines show the predominance field for a total Fe concentration of 500 µmol and a log(pCO_2/bar) of −1.0. The dashed black lines represent the ferrihydrite predominance field at the total Fe concentrations indicated in the figure. The dashed red lines illustrate the siderite predominance field at the log(pCO_2) values indicated by the red numbers in the plot at a Fe concentration of 500 µmol. The light orange field shows the extent of the predominance field of the $Fe(OH)_2^+$ species at 10 and 1 µmol Fe_{tot} concentrations. The average pH-Eh of rainwater, shown as a blue field labeled 'rain' was taken from Eiriksdottir et al. (2014).

found to be stable at these low sulfur concentrations and the pH-Eh of studied soil system.

3.3. Geochemical modelling

3.3.1. Mineral saturation states in the soil water samples

Calculated saturation indices of the sampled soil waters with respect to the 'On-Site' basaltic glass and common primary and secondary soil minerals at 7 °C are shown in Fig. 7. All the sampled soil solutions are saturated or supersaturated with respect to the SiO_2 polymorphs quartz and chalcedony, but undersaturated with respect to amorphous silica. Moganite is slightly undersaturated in all samples but closer to equilibrium than the other SiO_2 -phases.

The Al-Si-mineral allophane, the most common secondary mineral in Icelandic soils along with iron oxyhydroxides (Wada, 1989; Arnalds, 2004, 2015), is supersaturated at all depths, except for some of the samples collected at a depth of 76 cm. The silica-rich allophane, Al/Si1.26, is more supersaturated than the silica-poor allophanes. The Fe-Mg-rich smectite is undersaturated in all the shallow samples but close to saturation deeper in the soil (Fig. 7), while the Fe-Mg-poor smectite is only undersaturated at 76 cm and always supersaturated at deeper levels. The soil water samples are supersaturated with respect to ferrihydrite, except for some of the shallowest samples, which are undersaturated. Siderite ($FeCO_3$) and mackinawite (FeS) are undersaturated in the fluid samples at the shallowest depth, but close to saturation deeper in the soil. Amorphous FeS (not shown) and calcite are always undersaturated.

All fluid samples are undersaturated with respect to the main primary phases present in basalt, including 'On-Site' basaltic glass, which is consistent with the ongoing dissolution of the basaltic material throughout the soil column. The continuous undersaturation of the basaltic glass is due to the low concentrations of its dissolution products in the aqueous solution. The presence of organic acids also increases the degree of undersaturation of the Al-bearing primary minerals. In this way, the presence of DOC helps to accelerate the dissolution of the primary basaltic phases (Oelkers and Gislason, 2001).

3.3.2. Reaction path modelling

Reaction path models were run to 1) reproduce the soil water compositions measured in the field, 2) quantify the mass and volume of basalt dust dissolved, 3) predict the mass and volume of secondary phases, and 4) estimate the spatial variation in basalt dissolution and secondary mineral precipitation. The mass of basalt dissolved in the model calculation as a function of depth was determined by fitting the

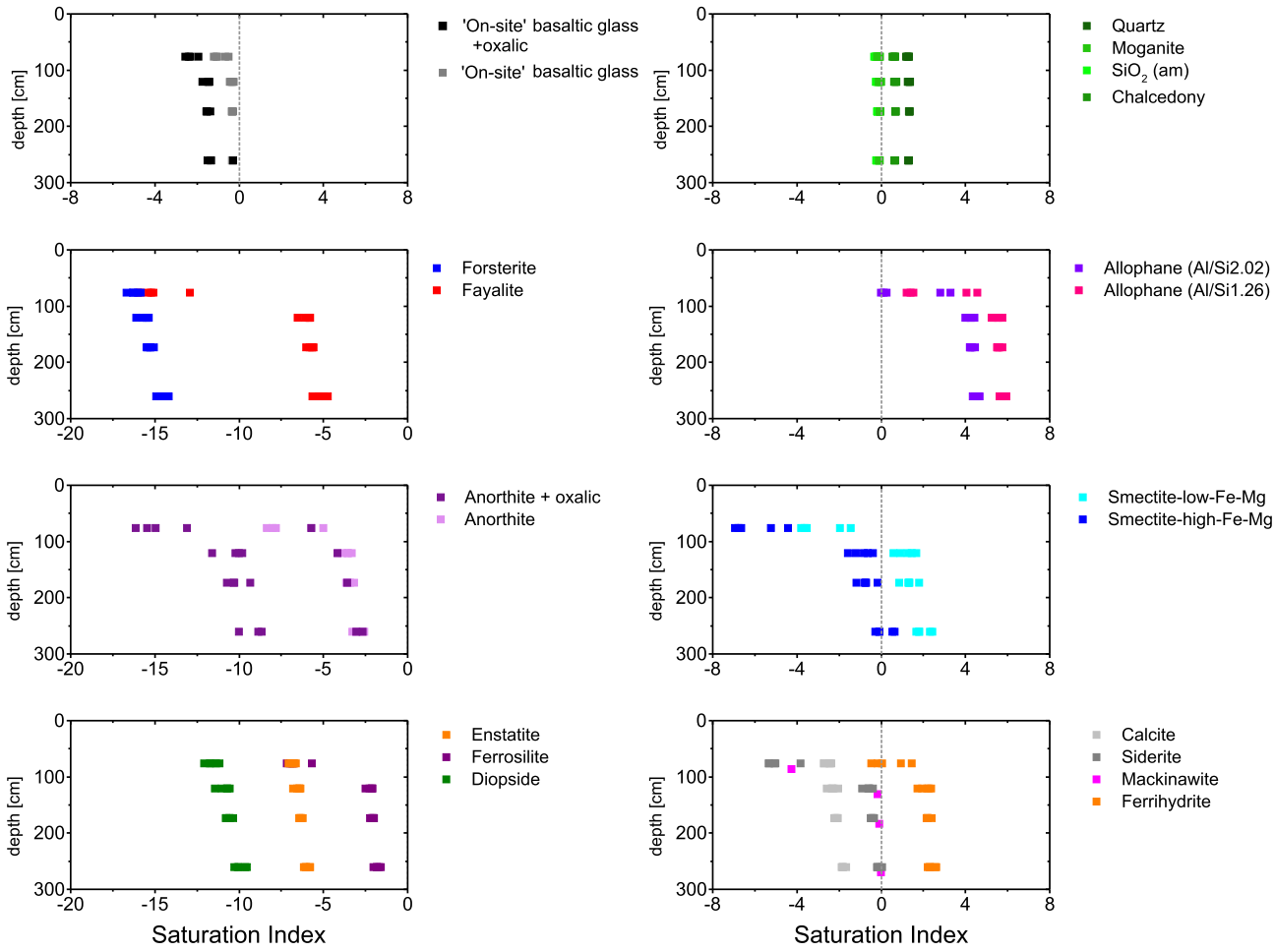

Fig. 7. Saturation indices of the sampled soil waters as a function of depth for primary basalt minerals on the left and for common secondary soil minerals on the right. The calculated saturation state of'On-Site' basaltic class and anorthite in the presence and absence of aqueous oxalate are both shown. The dashed vertical lines are consistent with fluid mineral equilibrium. The redox state used in the calculations is based on the measured fluid Fe^{2+}/Fe^{3+} and H_2S/S_{tot} ratios. Note the different scales on the various plots.

results of the calculation to the measured water compositions. The calculated soil water compositions as a function of depth obtained by this effort are illustrated as solid black curves in Fig. 4. A good agreement between the calculated curves and measured concentrations is evident.

As shown in the top left plot of Fig. 4, up to 260 mmol kg^{-1}_{water}, equal to ~310 mg kg^{-1}_{water}, of basalt needs to dissolve to reproduce the measured soil water compositions. This is equal to 0.26 cm^3 of basaltic glass per kg soil water solution. The dissolution of this basalt induces the precipitation of allophane, ferrihydrite, siderite and the silica polymorph moganite. The volume of each of these secondary minerals precipitated as a function of depth is illustrated in Fig. 8. The precipitation of these minerals has a complex influence on carbon uptake rates. Their precipitation maintains the aqueous fluid at undersaturated conditions with respect to the basaltic dust, promoting the dissolution of these solids. This precipitation can also alter fluid pH which can either increase or decrease the solubility of CO_2 in the aqueous phase.

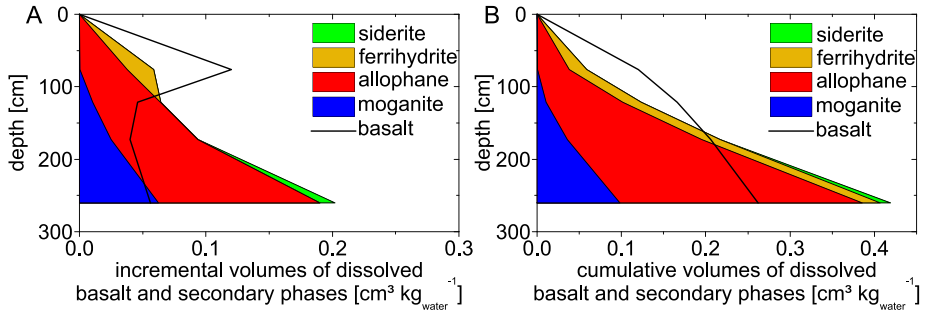

Fig. 8. Calculated volumes of minerals precipitated, and basalt dissolved per kg of soil solution A) incremental volume change and B) cumulative volume change from the top of the soil column to the indicated depth.

4. Discussion

4.1. Soil water chemistry and estimation of basalt dissolution rates

The measured soil waters are enriched in Si, Ca, Mg and Fe compared to rainwater. This confirms the dissolution of basalt in the soil. The breakdown of soil organic matter increases DOC and DIC concentration, as well as S and N, which are only present in low concentrations in the dissolving basalt. The pH of the water in this basalt-rich soil ranges from 5.8 to 6.7 and the alkalinity up to 3 meq kg^{-1}_{water}. In contrast, the alkalinity of water in corresponding organic-rich basaltic mineral-poor soils are commonly less than 0.3 meq kg^{-1}_{water} (Verry, 1975; Vitt et al., 1995). This comparison illustrates the ability of fine ground basalt dissolution to increase soil water alkalinity.

As the mass of sulfur in basalt is low (Wallace and Carmichael, 1992), it is likely that most of the S in the sampled soil water originated from the decomposition of organic material. Much of the sulfur in the organic material likely originated from sea spray, volcanic gas emissions, and global pollution. Organic decay occurs continuously with depth and organic matter decay releases sulfur (e.g., (Chen and Stevenson, 1986; Kirkby et al., 2011). It might be expected, therefore, that the total sulfur concentration in the soil waters will also increase with depth. Nevertheless, as shown in Fig. 5, total dissolved sulfur concentrations in the soil water decrease with depth, suggesting that aqueous S is being consumed by one or more solid phases. Based on the fluid saturation states, the most likely precipitating sulfide mineral at depth in the anoxic zone is mackinawite. The formation of this (or perhaps another) sulfide mineral likely helps scavenge some potentially toxic metals from the soil solutions via co-precipitation or sorption (see below and Rickard and Luther (2007); Swanner et al. (2019)).

The variation of soil water compositions as a function of depth allows estimation of the geometric surface area normalized dissolution rate of the 'On Site' basaltic glass in our studied soil. The dissolution rate, *r*, of this glass can be estimated taking account of (Oelkers and Gislason, 2001; Gislason and Oelkers, 2003)

$$r = \frac{1}{A_{geo}}\left(\frac{dm_{basalt}}{dm_{water}}\right)\left(\frac{dm_{water}}{dt}\right) \quad (3)$$

where A_{geo} corresponds to the total geometric surface area of basalt in the soil column, $\left(\frac{dm_{basalt}}{dm_{water}}\right)$ designates the mass of basalt dissolved into each incremental mass of water, and $\left(\frac{dm_{water}}{dt}\right)$ represents the rate at which water is passing through the soil column. Reactive path calculations suggest that up to ~310 mg kg^{-1}_{water} or ~$2.6x10^{-3}$ mol kg^{-1}_{water} of basaltic glass dissolved in our studied soil column. Correspondingly, the mass of water flowing through our soil system is estimated to be 925 ± 150 $kg_{water}\ m^{-2}\ yr^{-1}$.

The geometric surface area, A_{geo} in Eq. (3) is equal to the product of the specific surface area of the basaltic glass and its mass in the soil column. The specific geometric surface area, A'_{geo} can be estimated using (Brantley et al., 1999; Gautier et al., 2001).

$$A'_{geo} = \frac{6}{\rho \bullet d_{eff}} \quad (4)$$

where d_{eff} and ρ symbolize the effective grain diameter and the density of the basaltic glass, respectively. The effective particle size, d_{eff} can be determined from (Tester et al., 1994)

$$d_{eff} = \frac{d_{max} - d_{min}}{\ln\left(\frac{d_{max}}{d_{min}}\right)} \quad (5)$$

where d_{max} and d_{min} denote the maximum and minimum grain size of the basalt in the soil. A number of past studies concluded that most of the basaltic dust in Iceland is dominated by 10 to 62 μm size grains (Arnalds et al., 2014; Liu et al., 2014; Baldo et al., 2020). Based on these values, the effective diameter of the basalt grains is 28.5 μm. Taking account of Eq. (4) and a basaltic glass density of 2.7 t m^{-3}, the specific geometric surface area of the basaltic dust in our soil equals 78 $m^2\ kg^{-1}$.

The mass of basalt in the soil column is somewhat challenging to estimate. The soil contains approximately at least 50 % pore space (Snæbjörnsson, 1982) and up to 20 % organic carbon based on field observations (Arnalds, 2015). If it is assumed that half of the remaining volume is occupied by basalt, 15 percent of the volume of the soil is basalt and the remainder secondary minerals, including allophane and ferrihydrite. This estimate is roughly consistent with the current rate of basaltic glass input versus dissolution in the soil column. As mentioned above, the mass of basaltic dust in South Iceland can be a maximum of 0.8 kg $m^2\ yr^{-1}$. This flux is approximately 2.8 times the estimated rate of basalt dissolution in each m^2 of the soil column, which is estimated to be ~0.286 kg $m^2\ yr^{-1}$ by taking account of the mass of basalt dissolved annually in the soil column and the mass of water passing though this soil column.

Assuming the soil column contains 15 % basaltic glass by mass, the total volume of basalt in each square cm of the soil column is 40.5 cm^3, equal to 0.000045 m^3. This volume of basalt has a mass of 0.109 kg, such that the total surface area of basalt in the soil column equals 8.53 m^2. Taking account of this surface area together with the mass of basalt dissolving into each kg of water and the mass of water passing through the system, an estimate of the rate of basalt dissolution can be determined using Eq. (3), yielding a rate of $9x10^{-20}$ mol $m^2\ s^{-1}$. The uncertainty associated with this number is large owing to uncertainties in the mass and surface area of basalt in the soil column. Nevertheless, this field measured surface area normalized dissolution rate is approximately 2 orders of magnitude or more, slower than that measured in the laboratory at similar pH and temperature conditions, as reported by Oelkers and Gislason (2001) and Gislason and Oelkers (2003). Numerous past studies have reported that mineral reaction rates in the field are significantly slower than corresponding laboratory measured rates (Gislason and Arnórsson, 1993; White and Blum, 1995; White et al., 1996; White and Brantley, 2003; Molins et al., 2012). Numerous origins of this discrepancy have been proposed as summarized by White and Brantley (2003).

It should be emphasized that that both the large uncertainties in field-based weathering rates and large variations in annual environmental conditions including annual and seasonal temperature and rainfall patterns make it difficult to quantify carbon drawdown rates of proposed enhanced weathering efforts. Attempts to develop novel methods to overcome these limitations are currently ongoing (e.g., Kantola et al., 2023; Reershemis et al., 2023).

4.2. Toxic metal mobility

The mass of toxic metals released to the soil water in the study site by basalt dissolution can be estimated by taking account of the total mass of basalt dissolved in the system and the average composition of the dissolving basalt. To a first approximation the trace and toxic metal concentration of the basalt was taken to be equal to that of MORB as reported by Gale et al. (2013). The choice to use the composition of MORB in this instance is that it likely represents an average composition of the dust entering our system over time. Note because of annually and seasonally changes in wind direction, and of distinct volcanic eruptions, the trace element composition of dust arriving to our system is somewhat variable. The composition of MORB is also similar to that being considered for current enhanced rock weathering applications (Beerling et al., 2018). Taking this into account, the 0.31 g kgw^{-1} basaltic glass dissolved into the soil water would release ~245 nmol kg^{-1}_{water} Co, ~1600 nmol kg^{-1}_{water} Cr, ~390 nmol kg^{-1}_{water} Cu, ~525 nmol kg^{-1}_{water} Ni, and ~1 nmol kg^{-1}_{water} Pb, respectively. The concentration of each of these trace metals in the deepest collected soil waters are, however, lower by a factor of at least 5–200 relative to these values. This comparison

suggests that these trace metals have been reincorporated into the solid phase following their liberation from dissolving basalt. Note that this reduction in toxic trace element reduction may be underestimated as it does not take into account the potential remobilization of these elements from the secondary minerals in the soil. It is likely that the trace elements in our studied soil were originally sourced from the earlier dissolution of basaltic dust input.

The degree of depletion of selected major, toxic and trace metals in the collected soil waters are depicted in Fig. 9 relative to that of Ca. It is assumed that Ca is not incorporated into secondary phases. This choice is made due to the relatively high concentration of this element in the dissolving basalt, its low concentration in the influent rainwater, and the low stability of Ca-bearing secondary minerals in the studied system. Copper is the most depleted trace metal relative to its concentration in MORB, and chromium, nickel and cobalt are also strongly depleted at depth. Numerous past studies reported the incorporation of trace and toxic metals into iron oxyhydroxide phases (Scheinost et al., 2001; Brinza et al., 2008; Moon and Peacock, 2012) and into sulfide minerals (Rickard and Luther, 2007; Swanner et al., 2019). Both of these phases are predicted and/or observed to have formed in our studied soil system. Ferrihydrite was observed to have formed near the surface of our soil column, where the fluids are oxic, whereas mackinawite is predicted to have formed deeper in the soil column at anoxic conditions. The efficiency of scavenging toxic trace metals by secondary minerals in our studied system suggests that similar processes might limit toxic metal release from the waters discharged from geoengineered enhanced weathering systems.

Total dissolved Al is depleted in the fluids at all depth. Note that dissolved Al is highly toxic (Rosseland et al., 1992; Gensemer and Playle, 1999; Roy et al., 2000; Closset et al., 2021). Furthermore, the low concentration of Al^{3+} and potential complexation of this metal with aqueous organic species, ensures the continued dissolution of basaltic glass and plagioclase throughout the soil column. It can also be seen in Fig. 9 that Ca, Mg and Fe, dissolve near congruently at all depth, except for Fe at the shallowest level, which is at oxic conditions.

Due to secondary mineral scavenging, none of the soil water compositions contained metal concentrations that exceed the drinking water guidelines from the WHO, EPA or the Icelandic government, with the exception of Fe and Mn, (United States Environmental Protection Agency, 2009; Gunnarsdottir et al., 2016; World Health Organization, 2017). In all cases the trace and toxic metal concentrations were lower than the drinking water limits by at least a factor of 50. Nevertheless, the uptake of toxic trace elements by soils due to enhanced rock weathering

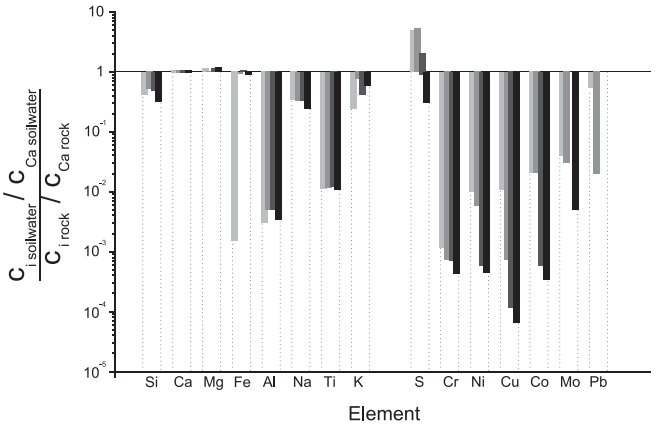

Fig. 9. The ratio of selected element concentrations normalized to Ca in the collected soil waters relative to the release from basalt assuming stoichiometric dissolution. All values have been corrected for seawater input. The shading of the columns indicates the depth of the water sample; the darker the shading, the deeper in the soil is the sample. The S concentration of MORB was taken from Wallace (2021) and trace metals from (Gale et al., 2013).

over time, eventually lead to soils accumulating metal contents that exceed environmental regulatory limits (Dupla et al., 2023).

4.3. Consequences for Enhanced Rock Weathering efforts

The results of this study have a number of implications for current enhanced weathering efforts. Notably, the enhanced weathering studies to date have added up to 400 t ha^{-1} (equal to 40,000 g m^{-2}) of ground basalt to soils (Gillman et al., 2002; Haque et al., 2019a). These efforts have only lasted for no more than several years. The present study, based on a natural analogue, provided insight into the long-term behavior of these efforts. Notably:

1. The basalt added annually to the soil of our study area does not totally dissolve each year. Only approximately half of the up to 800 g m^{-2} of basalt added annually to the soil is estimated to dissolve. Basalt and secondary minerals continue to accumulate in the soil over time. Results also suggest that basalt added up to 3300 years ago continues to dissolve in our studied soil system. Current ERW efforts typically add far more basalt annually than received by our study area, and the dust grains are also larger in size. It seems likely, therefore, that much of the basalt added in ERW efforts will persist long-term. Consequently, carbon drawdown by these efforts may not be as efficient as anticipated. Nevertheless, alkalinity production provoked by the addition of basalt to soils during ERW efforts will likely continue for significant time frames after the addition of the reactive material is terminated.
2. The dissolution of basaltic glass is observed to continue throughout the soil column. This observation favors the addition of reactive rock throughout the soil column, not just at the top of the soil. This continued dissolution is insured by the continued strong undersaturation of the soil waters with respect to primary basaltic minerals. This undersaturation is partially maintained by the decomposition of organic materials present in the soil column. This decomposition adds organic acid anions to the soil water, which helps maintain fluids at strongly undersaturated conditions.
3. The dissolution rates of basaltic glass are found to be approximately two orders of magnitude slower than corresponding laboratory rates. These slower field rates need to be taken into account when assessing the efficiency of enhanced weathering efforts.
4. Toxic and trace metals, likely released to the fluid phase by the dissolution of basaltic glass in our field area, are efficiently reincorporated into the soil column, likely by their coprecipitation and sorption into/to secondary minerals. Although this process assures that waters released from the soils into surface and groundwater systems will likely be non-toxic, these metals will build up in the soil profile. The degree to which the increasing content of trace and toxic metals in the soil column is detrimental to the local biota remains unclear.

5. Conclusions

This study focused on the fluid compositions and mineralogy of a natural soil that has received up to 800 g m^{-2} of basaltic dust annually for ~3300 years. Despite the dissolution of some of this basalt annually, it is estimated that more than half of the basalt added is still present in the studied soil column. The results of this field study, therefore, illuminate the potential and the limitations of ERW efforts. The precipitation of secondary minerals and the addition of organic acids maintains the soil waters undersaturated with respect to the primary minerals and glasses present in basalt. This assures the continued dissolution of basalt present in the soil system and suggests that the maximum total mass of basalt added to soil can be substantially greater than that of our studied soil system without slowing the specific dissolution rate of the basalt. Both this result and the observation that toxic metals are retained in the soil despite their likely release by dissolving basalts, encourages the

continued consideration of ERW for CO_2 drawdown from the atmosphere.

Nevertheless, this study also suggests some strong limitations to ERW efforts. Notably, basaltic glass dissolution rates are substantially lower than might be expected from laboratory experiments. This limits the near-term efficiency of such efforts. In addition, the long-term effect of the buildup of toxic and trace metals on soil ecosystems remains unresolved. Taken together these limitations compel new studies of natural analogue systems to further illuminate the long-term consequences of ERW efforts.

Funding

This project was funded by the European Union's Horizon 2020 research and innovation programme under the Marie Skłodowska-Curie grant agreement No 675219, from Landsvirkjun under the project number 2456, and the Icelandic Center for Research (Rannís) on behalf of the Doctoral Student Fund of the Ministry for the Environment and Natural Resources under the grant No 218929-051. This research used resources of the Advanced Photon Source, a U.S. Department of Energy (DOE) Office of Science User Facility operated for the DOE Office of Science by Argonne National Laboratory under Contract No. DE-AC02-06CH11357. This research was partly supported by research grant CRG9 2020 KAUST-UI.

Data availability

Data are available through Mendeley data at: https://doi.org/10.17632/cnxs8ztzsk.1.

Credit authorship contribution statement

T. Linke: Writing – review & editing, Writing – original draft, Visualization, Methodology, Investigation, Formal analysis, Data curation, Conceptualization. **E.H. Oelkers:** Writing – review & editing, Methodology, Conceptualization. **K. Dideriksen:** Methodology, Investigation. **S.C. Möckel:** Investigation. **S. Nilabh:** Investigation. **F. Grandia:** Investigation. **S.R. Gislason:** Writing – review & editing, Supervision, Project administration, Funding acquisition, Data curation, Conceptualization.

Declaration of competing interest

The authors declare that they have no known competing financial interests or personal relationships that could have appeared to influence the work reported in this paper.

Acknowledgement

We want to thank the Icelandic meteorological office (Veðurstofa Íslands) for providing rainwater data, Liane Benning and her team at the German research centre for Geosciences GFZ Potsdam for DOC measurements and Stephen Reid at the University of Leeds for ICP-MS analysis. Þorsteinn Jónsson for assistant in the field and design of various coring equipment and Egill Erlendsson and Guðrún Gísladóttir at University of Iceland for helping with the site selection. We would also like to thank Bryndís Róbertsdóttir at the National Energy Authority Iceland for her help with identifying the tephra layers and Eirikur Benjaminsson for access to his property containing the studied field side. We would like to thank Susan Stipp and Dominique Tobler, the MetalAid coordinators, as well as the network members for their help and pleasant company during this study. SRG and EHO would like to thank Hussein Hoteit and Abdulkader M. Alafifi at KAUST University, Saudi Arabia for their hospitality and support.

Appendix A. Supplementary material

Chemical compositions of the soil water samples are provided together with a figure showing their temporal evolution, as well as the Eh measured and derived from different redox couples in the supplementary material, as well as additions to the thermodynamic database and the rainwater composition used for the modeling and the calculations of the basalt dissolution rates. Supplementary material to this article can be found online at https://doi.org/10.1016/j.gca.2024.02.005.

References

Allison, J.D., Brown, D.S., Novo-Gradac, K.J., 1991. *MINTEQA2/PRODEFA2—A geochemical assessment model for environmental systems—Version 3.0 user's manual.*, Athens, Georgia 30605.

Amann, T., Hartmann, J., Struyf, E., De Oliveira Garcia, W., Fischer, E.K., Janssens, I., Meire, P., Schoelynck, J., 2018. Constraints on Enhanced Weathering and related carbon sequestration-a cropland mesocosm approach. Biogeosci. Discuss. 1–21.

Arnalds, O., 2004. Volcanic soils of Iceland. Catena (Amst) 56, 3–20.

Arnalds, O., 2010. Dust sources and deposition of aeolian materials in Iceland. Icel. Agric. Sci. 23, 3–21.

Arnalds, O., 2015. The Soils of Iceland. Springer, Netherlands, Dordrecht.

Arnalds, O., Olafsson, H., Dagsson-Waldhauserova, P., 2014. Quantification of iron-rich volcanogenic dust emissions and deposition over the ocean from Icelandic dust sources. Biogeosciences 11, 6623–6632.

Arnalds, O., Dagsson-Waldhauserova, P., Olafsson, H., 2016. The Icelandic volcanic aeolian environment: processes and impacts - A review. Aeolian Res. 20, 176–195.

Arnórsson, S., 2000. Isotopic and Chemical Techniques in Geothermal Exploration, Development and Use. In: Arnórsson, S. (Eds.) International Atomic Energy Agency, Vienna.

Baek, S.H., Kanzaki, Y., Lora, J.M., Planavsky, N., Reinhard, C.T., Zhang, S., 2023. Inpact of climate on the global capacity for enhances rock weathering on croplands. Earth's Future 11, e2023EF003698.

Baldo, C., Formenti, P., Nowak, S., Chevaillier, S., Cazaunau, M., Pangui, E., Di Biagio, C., Doussin, J.F., Ignatyev, K., Dagsson-Waldhauserova, P., Arnalds, O., Mackenzie, A.R., Shi, Z., 2020. Distinct chemical and mineralogical composition of Icelandic dust compared to northern African and Asian dust. Atmos. Chem. Phys. 20, 13521–13539.

Beerling, D.J., Leake, J.R., Long, S.P., Scholes, J.D., Ton, J., Nelson, P.N., Bird, M., Kantzas, E., Taylor, L.L., Sarkar, B., Kelland, M., DeLucia, E., Kantola, I., Müller, C., Rau, G., Hansen, J., 2018. Farming with crops and rocks to address global climate, food and soil security. Nat. Plants 4, 138–147.

Beerling, D.J., Kantzas, E.P., Lomas, M.R., Wade, P., Eufrasio, R.M., Renforth, P., Sarkar, B., Andrews, M.G., James, R.H., Pearce, C.R., Mercure, J.F., Pollitt, H., Holden, P.B., Edwards, N.R., Khanna, M., Koh, L., Quegan, S., Pidgeon, N.F., Janssens, I.A., Hansen, J., Banwart, S.A., 2020. Potential for large-scale CO_2 removal via enhanced rock weathering with croplands. Nature 583, 242–248.

Brantley, S.L., White, A.F., Hodson, M., 1999. Surface Area of Primary Silicate Minerals. In: Jamtveit, B., Meakin, P. (Eds.), Growth and Dissolution in Geosystems. Kluwer Academic Publishers, Dordrecht, pp. 291–326.

Brinza, L., Benning, L.G., Statham, P.J., 2008. Adsorption studies of Mo and Vonto ferrihydrite. Mineral. Mag. 72, 385–388.

Charriau, A., Lesven, L., Gao, Y., Leermakers, M., Baeyens, W., Ouddane, B., Billon, G., 2011. Trace metal behaviour in riverine sediments: role of organic matter and sulfides. Appl. Geochem. 26, 80–90.

Chen, Y., Stevenson, F.J., 1986. Soil organic matter interactions with trace elements. In: Chen, Y., Avnimelech, Y. (Eds.), The Role of Organic Matter in Modern Agriculture. Springer, Dordrecht, pp. 73–116.

Cho, Y., Driscoll, C.T., Johnson, C.E., Siccama, T.G., 2010. Chemical changes in soil and soil solution after calcium silicate addition to a northern hardwood forest. Biogeochemistry 100, 3–20.

Closset, M., Cailliau, K., Slaby, S., Marin, M., 2021. Effects of aluminium contamination on the nervous system of freshwater aquatic vertebrates: a review. Int. J. Mol. Sci. 23, 31.

Deng, H., Sonnenthal, E., Arora, B., Breuning, H., Brodie, E., Kleber, M., Spycher, N., Nico, P., 2023. The environmental controls on efficiency of enhaced rock weathering. Sci. Rep. 13, 9765.

Dideriksen, K., Frandsen, C., Bovet, N., Wallace, A.F., Sel, O., Arbour, T., Navrotsky, A., De Yoreo, J.J., Banfield, J.F., 2015. Formation and transformation of a short range ordered iron carbonate precursor. Geochim. Cosmochim. Acta 164, 94–109.

Dietzen, C., Harrison, R., Michelsen-Correa, S., 2018. Effectiveness of enhanced mineral weathering as a carbon sequestration tool and alternative to agricultural lime: an incubation experiment. Int. J. Greenhouse Gas Cont. 74, 251–258.

Dupla, X., Möller, B., Baveye, P.C., Grand, S., 2023. Potential accumulation of toxic trace elements in soils during enhanced rock weathering. Eur. J. Soil Sci. 74, e13343.

Edwards, D.P., Lim, F., James, R.H., Pearce, C.R., Scholes, J., Freckleton, R.P., Beerling, D.J., 2017. Climate change mitigation: potential benefits and pitfalls of enhanced rock weathering in tropical agriculture. Biol. Lett. 13.

Effenberger, H., Mereiter, K., Zemann, J., 1981. Crystal structure refinements of magnesite, calcite, rhodochrosite, siderite, smithonite, and dolomite, with discussion

of some aspects of the stereochemistry of calcite type carbonates. Z Kristallogr Cryst. Mater. 156, 233–244.
Eiriksdottir, E.S., Sigurdsson, Á., Gislason, S.R., Torssander, P., 2014. Chemical composition of precipitation and river water in southern iceland: effects of Eyjafjallajökull volcanic eruptions and geothermal power plants. Procedia Earth Planet. Sci. 10, 358–364.
Eswaran, H., van den Berg, E., Reich, P., 1993. Organic carbon in soils of the world. Soil Sci. Soc. Am. J. 57, 192–194.
Gale, A., Dalton, C.A., Langmuir, C.H., Su, Y., Schilling, J.G., 2013. The mean composition of ocean ridge basalts. Geochem. Geophys. 14, 489–518.
Gautier, J.M., Oelkers, E.H., Schott, J., 2001. Are quartz dissolution rates proportional to B.E.T. surface areas? Geochim. Cosmochim. Acta 65, 1059–1070.
Gensemer, R.W., Playle, R.C., 1999. The bioavailability and toxicity of aluminum in aquatic environments. Crit. Rev. Environ. Sci. Technol. 29, 315–450.
Gillman, G.P., Burkett, D.C., Coventry, R.J., 2002. Amending highly weathered soils with finely ground basalt rock. Appl. Geochem. 17, 987–1001.
Gislason, S.R., Arnórsson, S., 1993. Dissolution of primary basaltic minerals in natural waters: saturation state and kinetics. Chem. Geol. 105, 117–135.
Gislason, S.R., Oelkers, E.H., 2003. Mechanism, rates, and consequences of basaltic glass dissolution: II. An experimental study of the dissolution rates of basaltic glass as a function of pH and temperature. Geochim. Cosmochim. Acta 67, 3817–3832.
Goll, D.S., Ciais, P., Amann, T., Buermann, W., Chang, J., Eker, S., Hartmann, J., Janssens, I., Li, W., Obersteiner, M., Penuelas, J., Tanaka, K., Vicca, S., 2021. Potential CO_2 removal from enhanced weathering by ecosystem responses to powdered rock. Nat. Geosci. 14, 545–549.
Gran, G., 1952. Determination of the equivalence point in potentiometric Titrations. Part II. Analyst 77, 661–671.
Gunnarsdottir, M.J., Gardarsson, S.M., Jonsson, G.S., Bartram, J., 2016. Chemical quality and regulatory compliance of drinking water in Iceland. Int. J. Hyg. Environ. Health 219, 724–733.
Hammersley, A.P., Svensson, S.O., Hanfland, M., Fitch, A.N., Häusermann, D., 1996. Two-dimensional detector software: from real detector to idealised image or two-theta scan. High Press Res. 14, 235–248.
Hammersley, A.P., 1997. FIT2D: An Introduction and Overview., Grenoble, ESRF Internal Report, ESRF97HA02T.
Haque, F., Chiang, Y., Santos, R., 2019a. Alkaline mineral soil amendment: a climate change 'stabilization wedge'? Energies 12, 2299.
Haque, F., Santos, R.M., Dutta, A., Thimmanagari, M., Chiang, Y.W., 2019b. Co-benefits of wollastonite weathering in agriculture: CO_2 sequestration and promoted plant growth. ACS Omega 4, 1425–1433.
Haque, F., Santos, R.M., Chiang, Y.W., 2020. Optimizing inorganic carbon sequestration and crop yield with Wollastonite soil amendment in a microplot study. Front. Plant Sci. 11, 1012.
Haque, F., Santos, R.M., Chiang, Y.W., 2021. Urban farming with enhanced rock weathering as a prospective climate stabilization wedge. Cite This: Environ. Sci. Technol. 55, 13575–13578.
Harðardóttir, S., 2020. Spatial distribution and geochemical characterization of Icelandic mantle end-members. MSc Thesis, University of Iceland.
Hartmann, J., West, A.J., Renforth, P., Köhler, P., De La Rocha, C.L., Wolf-Gladrow, D.A., Dürr, H.H., Scheffran, J., 2013. Enhanced chemical weathering as a geoengineering strategy to reduce atmospheric carbon dioxide, supply nutrients, and mitigate ocean acidification. Rev. Geophys. 51, 113–149.
Huber, S.A., Balz, A., Abert, M., Pronk, W., 2011. Characterisation of aquatic humic and non-humic matter with size-exclusion chromatography - organic carbon detection - organic nitrogen detection (LC-OCD-OND). Water Res. 45, 879–885.
IPCC (2018) *Global warming of 1.5°C An IPCC Special Report on the impacts of global warming of 1.5°C above pre-industrial levels and related global greenhouse gas emission pathways, in the context of strengthening the global response to the threat of climate change, sustainable development, and efforts to eradicate poverty*. Masson-Delmotte, V., Zhai, P., Pörtner, H.-O., Roberts, D., Skea, J., Shukla, P.R., Pirani, A., Moufouma-Okia, W., Péan, C., Pidcock, R., Connors, S., Matthews, J.B.R., Chen, Y., Zhou, X., Gomis, M.I., Lonnoy, E., Maycock, T., Tignor, M., Waterfield, T. (Eds.), Cambridge University Press, Cambridge, UK and New York, NY, USA, pp. 3–24.
Kaasalainen, H., Stefánsson, A., Druschel, G.K., 2016. Determination of Fe(II), Fe(III) and Fetotal in thermal water by ion chromatography spectrophotometry (IC-Vis). Int. J. Environ. Anal. Chem. 96, 1074–1090.
Kantola, I.B., Blanc-Betes, E., Master, M.D., Chang, E., Marklein, A., Moore, C.E., von Haden, A., Bernacchi, C.J., Wolf, A., Epihov, D.Z., Beerling, D.J., DeLucia, E.H., 2023. Improved net carbon budgets in the US Mlidwest through direct measured impacts of enhanced weatehring. Globl. Chang Biol. 29, 7012–7028.
Kantzas, E.P., Val Martin, M., Lomas, M.R., Eufrasio, R.M., Renforth, P., Lewis, A.L., Taylor, L.L., Mecure, J.F., Pollitt, H., Vercoulen, P.V., Vakilifard, N., Holden, P.B., Edwards, N.R., Koh, L., Pidgeon, N.F., Banwart, S.A., Beerling, D.J., 2022. Substantial carbon drawdown potential from enhanced rock weathering in the United Kingdom. Nat. Geosci. 15, 382–389.
Kinniburgh, D.G., Cooper, D.M., 2004. Predominace and mineral stability diagrams revisited. Environ. Sci. Tech. 38, 3641–3648.
Kirkby, C.A., Kirkegaard, J.A., Richardson, A.E., Wade, L.J., Blanchard, C., Batten, G., 2011. Stable soil organic matter: A comparison of C:N:P: S ratios in Australian and other world soils. Geoderma 163, 197–208.
Linke, T., Gislason, S.R., 2018. Stability of iron minerals in Icelandic peat areas and transport of heavy metals and nutrients across oxidation and salinity gradients - A modelling approach. Energy Procedia 146, 30–37.
Liu, E.J., Cashman, K.V., Beckett, F.M., Witham, C.S., Leadbetter, S.J., Hort, M.C., Guðmundsson, S., 2014. Ash mists and brown snow: Remobilization of volcanic ash from recent Icelandic eruptions. J. Geophys. Res. Atmos. 119, 9463–9480.
Molins, S., Trebotich, D., Steefel, C.I., Shen, C., 2012. An investigation of the effect of pore scale flow on average geochemical reaction rates using direct numerical simulation. Water Resour. Res. 48, W03527.
Moon, E.M., Peacock, C.L., 2012. Adsorption of Cu(II) to ferrihydrite and ferrihydrite-bacteria composites: Importance of the carboxyl group for Cu mobility in natural environments. Geochim. Cosmochim. Acta 92, 203–219.
Moosdorf, N., Renforth, P., Hartmann, J., 2014. Carbon dioxide efficiency of terrestrial enhanced weathering. Environ. Sci. Tech. 48, 4809–4816.
Oelkers, E.H., Gislason, S.R., 2001. Mechanism, rates, and consequences of basaltic glass dissolution: I.An experimental study of the dissolution rates of basaltic glass as a function of aqueous Al, Si and oxalic acid concentration at 25°C and pH ? 3 and 11. Geochim. Cosmochim. Acta 67, 3817–3832.
Parkhurst, D.L., Appelo, C.A.J., 1999. User's Guide to PHREEQC (Version 2)— A Computer Program for Speciation, Batch-Reaction, One-Dimensional Transport, and Inverse Geochemical Calculations., U.S. Geological Survey, Water Resources Investigations Report 99-4259, Washington DC.
Paulo, C., Power, I.M., Stubbs, A.R., Wang, B., Zeyen, N., Wilson, S., 2021. Evaluating feedstocks for carbon dioxide removal by enhanced rock weathering and CO_2 mineralization. App. Geochem. 129, 104955.
Petersen, G.N., Berber, D., 2018. Jarðvegshitamælingar á Íslandi. Staða núverandi kerfis og framtíðarsýn., VÍ 2018-009.
Pettit, L.D., Powell, J.J., 2008. The IUPAC Stability Constants Database (SC-Database), current data version 4, Academic Software., Otley, UK.
Qiu, X., Thompson, J.W., Billinge, S.J.L., 2004. PDFgetX2: a GUI-driven program to obtain the pair distribution function from X-ray powder diffraction data. J. Appl. Cryst. 37, 678.
Reershemius, T., Kelland, M.E., Jordan, J.S., Davis, I.R., D'Ascanio, R., Kalderon-Asael, B., Asael, D., Suhrhoff, T.J., Epihov, D.Z., Beerling, D.J., Reinhard, C.T., Planavsky, N.J., 2023. Initial validaion of a soil-based mass-balance approach for empirical monitoring of enhanced rock weathering rates. Environ. Sci. Technol. 57, 19497–19507.
Rickard, D., Luther, G.W., 2007. Chemistry of Iron Sulfides. Chem. Rev. 107, 514–562.
Rosseland, B.O., Blakar, I.A., Bulger, A., Kroglund, F., Kvellstad, A., Lydersen, E., Oughton, D.H., Salbu, B., Staurnes, M., Vogt, R., 1992. The mixing zone between limed and acidic river waters: complex aluminium chemistry and extreme toxicity for salmonids. Environ. Pollut. 78, 3–8.
Roy, R.L., Campbell, P.G.C., Prémont, S., Labrie, J., 2000. Geochemistry and toxicity of aluminum in the saguenay river, québec, Canada, in relation to discharges from an aluminum smelter. Environ. Toxicol. Chem. 19, 2457–2466.
Sawyer, D.T., Roberts, J.L., Sobkowiak, A., 1995. Electrochemistry for Chemists, 2nd ed. Wiley, New York.
Scheinost, A.C., Abend, S., Pandya, K.I., Sparks, D.L., 2001. Kinetic controls on Cu and Pb sorption by ferrihydrite. Environ. Sci. Tech. 35, 1090–1096.
Schuiling, R.D., Krijgsman, P., 2006. Enhanced weathering: an effective and cheap tool to sequester CO_2. Clim. Change 74, 349–354.
Smieja-Król, B., Janeczek, J., Bauerek, A., Thorseth, I.H., 2015. The role of authigenic sulfides in immobilization of potentially toxic metals in the Bagno Bory wetland, southern Poland. Environ. Sci. Pollut. Res. 22, 15495–15505.
Snæbjörnsson, Á., 1982. Um Vatnsleiðnimælingar í Jarðvegi á nokkrum stöðum í Borgarfirði. Fjölrit 45, 35.
Swanner, E.D., Webb, S.M., Kappler, A., 2019. Fate of cobalt and nickel in mackinawite during diagenetic pyrite formation. Am Min 104, 917–928.
ten Berge, H.F.M., van der Meer, H.G., Steenhuizen, J.W., Goedhart, P.W., Knops, P., Verhagen, J., 2012. Olivine weathering in soil, and its effects on growth and nutrient uptake in ryegrass (Lolium perenne L.): a pot experiment. PLoS One. 7.
Tester, J.W., Worley, W.G., Robinson, B.A., Grigsby, C.O., Feerer, J.L., 1994. Correlating quartz dissolution kinetics in pure water from 25 to 625°C. Geochim. Cosmochim. Acta 58, 2407–2420.
U.S. Environmental Protection Agency, 1998. MINTEQA2/PRODEFA2, A Geochemical Assessment Model for Environmental Systems: User Manual Supplement for Version 4.0., Athens, Georgia.
United States Environmental Protection Agency, 2009. National Primary Drinking Water Guidelines. *Epa 816-F-09-004* **1**, United States Environmental Protection Agency. 7p.
Verry, E., 1975. Streamflow chemistry and nutrient yields from upland-peatland watersheds in Minnesota. Ecology 56, 1149–1157.
Vitt, D.H., Bayley, S.E., Jin, T.-L., 1995. Seasonal variation in water chemistry over a bog-rich fen gradient in Continental Western Canada. Can. J. Fish Aquat. 52, 587–606.
Wada, K., 1989. Allophane and Imogolite. In: Dixon, J.B., Weed, S.B. (Eds.), Minerals in Soil Environments, second ed. Soil Science Society of America, Madison, pp. 1051–1087.
Wallace, P., Carmichael, I.S.E., 1992. Sulfur in basaltic magmas. Geochim. Cosmochim. Acta 56, 1863–1874.
Wallace, P.J., 2021. Magmatic Volatiles. In: Encyclopedia of Geology. Elsevier. pp. 301–312.
White, A.F., Blum, A.E., 1995. Effects of climate on chemical, weathering in watersheds. Geoch Cosmochim Acta 59, 1729–1747.
White, A.F., Blum, A.E., Schulz, S., Bullen, T.D., Harden, J.W., Peterson, M.L., 1996. Chemical weathering rates of a soil chronosequence on granitic alluvium: I. Quantification of mineralogical and surface area changes and calculation of primary silicate reaction rates. Geochim. Cosmochim. Acta 60, 2533–2550.
White, A.F., Brantley, S.L., 2003. The effect of time on the weathering of silicate minerals: why do weathering rates differ in the laboratory and field? Chem. Geol. 202, 479–506.
World Health Organization, 2017. Guidelines for Drinking-water Quality: fourth edition incorporating the first addendum, Licence: CC BY-NC-SA 3.0 IGO., Icelandic

Meteorological Office, Climatological data, annual averages of precipitation. http://www.en.vedur.is/climatology/data (accessed 15 Oct. 2021).